Proceedings of Global Power and Propulsion Society
ISSN-Nr: 2504-4400
GPPS Xi'an21
18th – 20th October, 2021
www.gpps.global

GPPS-TC-2021-0123

The mechanism of axial arrangement affecting the performance for tandem rotor with partial-height booster rotor in high-throughflow fan

Chuangxin ZHOU
Institute of Engineering Thermophysics, Chinese Academy of Sciences
University of Chinese Academy of Sciences
Innovation Academy for Light-duty Gas Turbine, Chinese Academy of Sciences
zhouchuangxin@iet.cn
Beijing, China

Shengfeng ZHAO
Institute of Engineering Thermophysics, Chinese Academy of Sciences
zhaoshengfeng@iet.cn
Beijing, China

Chengwu YANG
Institute of Engineering Thermophysics, Chinese Academy of Sciences
yangchengwu@iet.cn
Beijing, China

Ge HAN
Institute of Engineering Thermophysics, Chinese Academy of Sciences
hange@iet.cn
Beijing, China

Xingen LU
Institute of Engineering Thermophysics, Chinese Academy of Sciences
xingenlu@hotmail.com
Beijing, China

ABSTRACT

The high-throughflow fan is a novel fan stage configuration, in which the tandem rotor is composed of a partial-height booster rotor (*BR*) and a fan rotor (*FR*). Compared with the conventional fan stage, it can effectively improve the throughflow capacity and core pressurization ability. However, its axial matching characteristic has not been clarified and lacks engineering design principles. Therefore, this paper conducted a detailed numerical simulation study to investigate the effects of the axial arrangement on the aerodynamic performance and inner flow mechanisms of the tandem rotor in high-throughflow fan. The results demonstrate that the design parameter, namely axial overlap (*AO*), determines the overall performance of the fan stage, and has a significant impact on the flow structures of the tandem rotor at the peak efficiency condition (*PE*), such as the passage shock wave of the *FR*, which leads to being different in the isentropic efficiency (η).

INTRODUCTION

Enhancing the throughflow capacity of turbofan engines to improve their thrust-to-weight ratio, propulsion efficiency, and fuel economy has been an important trend in their development in recent years. As a core and complicated component of the turbofan engine, the fan directly determines the weight, specific fuel consumption, noise, and other performance parameters of the overall machine.

Tandem blades are widely studied in centrifugal compressors (Li et al., 2019; Li et al., 2020a; Li et al., 2020b) and axial compressors (Wu et al., 1988; Saha et al., 1997; Li et al., 2010) due to such characteristics as high loading, high efficiency, and wide margin. Researches on the tandem rotor of axial compressors began in the 1970s (Brent and Clemmons, 1974; Burger and Keenan, 1970). Subsonic tandem rotor has been developed rapidly due to the relatively uncomplicated internal flow in the blade channel. McGlumphy et al. (2010) investigated the subsonic tandem rotors for a core compressor rotor, which η was 91% with a loading coefficient of 0.55. Kumar and Pradeep (2019) further conducted the study of design and off-design behaviors, such as the gap-nozzle flow and the tip leakage vortex, et al, of a subsonic tandem rotor stage. Compared with the conventional stage, η was increased by 2.3% with the premise of the total pressure ratio (π) was enhanced by 3.6%. However, shock waves pose a challenge to the design of the tandem blades in transonic conditions. With the development of three-dimensional (3D) design techniques, namely the lean and sweep, the aerodynamic performance of transonic tandem rotors had been significantly improved. Mohsen et al. (2017) divided NASA Rotor 37

into a tandem rotor, then improved the design, and the π and η were increased by 17% and 2% compared with the baseline respectively.

To decrease the weight of the fan stage, Murooka et al. (2007) proposed a novel fan configuration where a partial-height *BR* was installed in front of the *FR* in a tandem rotor design. Zhou et al. (2021) further explored the circumferential relative position of the *BR* and *FR* inside the tandem rotor and discussed the mechanisms of the internal flow. The axial arrangement in the tandem rotor is also important. However, there is no study to date has examined the axial design parameters of the high-throughflow fan.

In the above research backdrop, this study designs and uses a high-throughflow fan as the research object. Numerical simulations are then used to examine the influence of AO on the aerodynamic performance of the fan stage and tandem rotor. This study also clarifies the mechanisms of the changes in typical flow structures inside the compressor with the relative positions of the BR and FR and provides basic theoretical guidance for the aerodynamic design and engineering applications of the high-throughflow fan.

STUDY CASES OF HIGH-THROUGHFLOW FAN

The high-throughflow fan consisted of three blade rows: a partial-height *BR*, a wide-chord compound-sweep *FR*, and a back-sweep end-bending stator, which was a novel fan configuration compared with the conventional fan. The *BR* and *FR* formed a tandem rotor concept to effectively improve the throughflow and the core pressurization capacity of the fan. The 3D structure and meridional schematic figure of the high-throughflow fan were shown in Figure 1, and some key geometric and aerodynamic parameters were shown in Table 1.

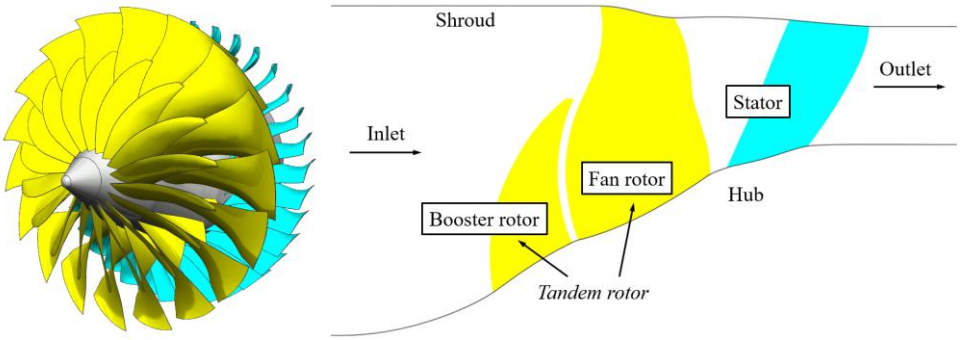

Figure 1 The 3D Structure and meridional schematic diagram of high-throughflow fan

Table 1 Key geometric and aerodynamic parameters

Parameter	Value
Design choke mass flow	37 (kg/s)
Design total pressure ratio	2.05
Number of blades	18-18-35
Hub-to-tip ratio at inlet	0.32
Mass flow per unit aera at inlet	217 (kg/s/m^2)
Relative Mach number at inlet tip	1.53

Different from the conventional fan, the novel fan introduced two more design parameters inside the tandem rotor: the axial relative position parameter, namely *AO*, and the circumferential relative position parameter, namely percent pitch (*PP*), respectively. They were demonstrated in Figure 2 and defined as

$$AO = \Delta x / C_x . \quad (1)$$

$$PP = s / t . \quad (2)$$

where Δx represented the axial distance between the trailing edge (*TE*) of the *BR* and the leading edge (*LE*) of the *FR*, C_x represented the axial chord length of the *BR*, s represented the circumferential distance between the chordwise extension of the *BR* and the *LE* of the *FR*, and t was the blade pitch of the *BR*. Since the C_x varied greatly from hub to tip, it was regarded as the spanwise averaged C_x when calculating different *AO*. It meant that there was an axial gap between the *BR* and *FR* when *AO* was positive, and an axial overlap between the *BR* and *FR* when *AO* was negative. And it meant that the *PS* of *BR* was closer to the *SS* of *FR* in the circumferential direction when *PP* was relatively small and far away from the *SS* of *FR* when *PP* was large. The main purpose of the current study was to investigate the effects of *AO* on the aerodynamic performance and internal mechanism. Therefore, *PP* was fixed at 20%, which would make the tandem rotor reach better performance, and *AO* were valued +10%, +5%, 0%, -5% and -10%, respectively.

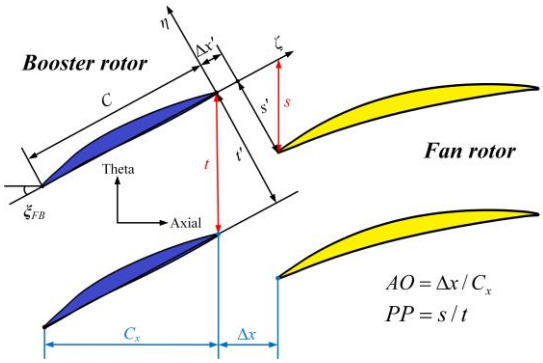

Figure 2 Schematic diagram of the key design parameters inside tandem rotor

NUMERICAL METHODOLOGY

To estimate the performance and obtain the inner flow field of the high-throughflow fan precisely, the commercial software ANSYS CFX was applied to the numerical simulation in the current study. The shear stress transport (SST) turbulence model was used to solve the transport of shear stress in the full 3D steady-state Navier-Stokes equations, and the high-resolution scheme was applied to account for the convection term to ensure accuracy. The inlet was set to be the total pressure and total temperature boundary condition (101325 Pa, 288.15 K), and the inflow direction was imposed as the fully axial. Except for the rotor blade surfaces and their connected hub rotated, the other endwalls were set to be stationary, and the all surfaces were fixed as the adiabatic and non-slip boundary conditions. The mixing plane method was applied to transfer the flow message between the tandem rotor domain and the stator domain. The outlet was set to be the averaged static pressure boundary condition, and the performance curve was obtained by gradually increasing the outlet static pressure until the calculation unable to be convergent.

The block-structured grids generated by the automatic grid generator software NUMECA IGG/Autogrid 5 were applied for the numerical simulation. The grids of the tandem rotor domain and the stator domain were produced independently, and the full matching grids were used in the passage of the tandem rotor. The HOH topology was applied for the blade surfaces and the O4H topology was applied for the tip clearance of the *BR* and *FR*. Since the requirement of the turbulence model, the non-dimensional height of the first layer mesh of the wall y^+ should equal approximately one. The final grids and some details were demonstrated in Figure 3.

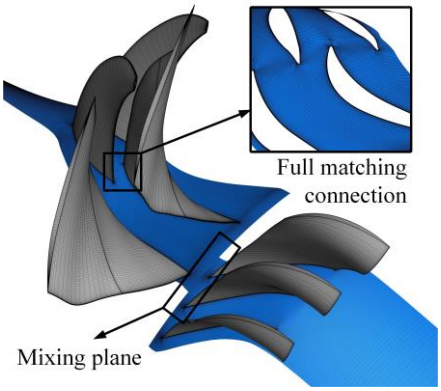

Figure 3 Numerical simulation grids

The high-throughflow fan was developed from the conventional fan which designed and tested by the Institute of Engineering Thermophysics of the Chinese Academy of Sciences. Therefore, the numerical simulation methodology should be verified first before exploring the influence of *AO* on aerodynamic performance, and the results were shown in Figure 4. The mass flow was non-dimensionalized by the corresponding choke mass flow of the experiment and the simulation at 100% rotation speed. The π and η were usually applied to estimate the performance of the compressor, and they were defined as

$$\pi = P_{t,outlet} / P_{t,inlet} \ . \qquad (3)$$

$$\eta = \frac{\pi^{\frac{\gamma-1}{\gamma}} - 1}{T_{t,outlet} / T_{t,inlet} - 1} . \qquad (4)$$

where $P_{t,outlet}$ represented the outlet total pressure of the tandem rotor or the fan stage, $P_{t,inlet}$ represented the inlet total pressure of the fan stage, γ represented the specific heat ratio, $T_{t,outlet}$ represented the outlet total temperature of the tandem

rotor or the fan stage, $T_{t,inlet}$ represented the inlet total temperature of the fan stage. Figure 4 showed that the value and the variation trend of π from near choke condition to the near stall condition obtained by the numerical simulation, which were consistent with the experimental data, and confirmed the reliability of the methodology in the current study.

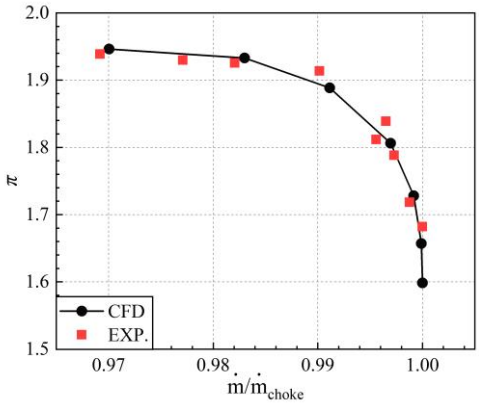

Figure 4 Verification of the numerical simulation methodology

RESULTS AND DISCUSSION

Influence of *AO* on aerodynamic performance

To explore the effects of *AO* on high-throughflow fan aerodynamic performance, the performance curves with different *AO* should be obtained first, which were shown in Figure 5. The mass flow ($\dot{m}$) was non-dimensionalized by the design choke mass flow ($\dot{m}_{design}$) mentioned in Table 1. It could be observed from Figure 5 that π and η of the overall fan stage varied obviously with reduced *AO*, and the variation trend of performance was continuously decreased. Therefore, *AO* was one of the most important parameters during the compressor design.

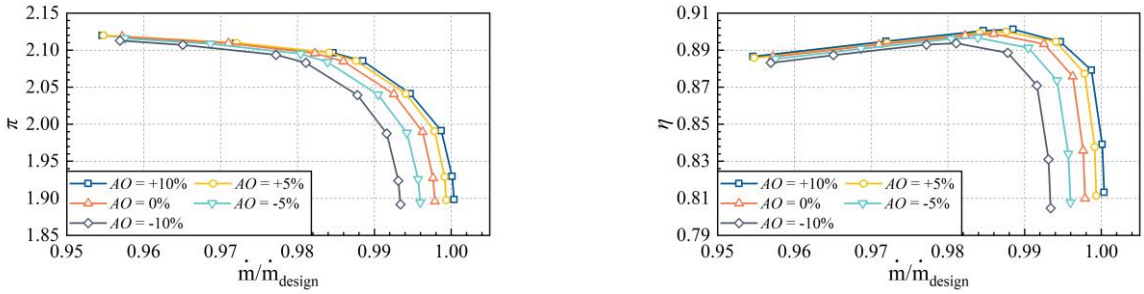

Figure 5 The performance curve of fan stage with different *AO*

To demonstrate clearly and analyze deeply, we further selected the performance at *PE* (outlet static pressure equaled 163 kPa) to compare. As shown in Figure 6, η was reduced with decreased *AO* and would be a non-linear variation trend when *AO* was negative (that is, *BR* and *FR* were overlapped in axial). Not only that, the difference of η between the best case (*AO* = +10%) and the worst case (*AO* = -10%) was 0.756%, thus, the larger *AO* should be selected during the high-throughflow fan design. Different from the variation trend of η, π was almost maintained to be unchanged with various *AO*. As a result, it indicated that *AO* could greatly change η, however, π was insensitive with *AO*.

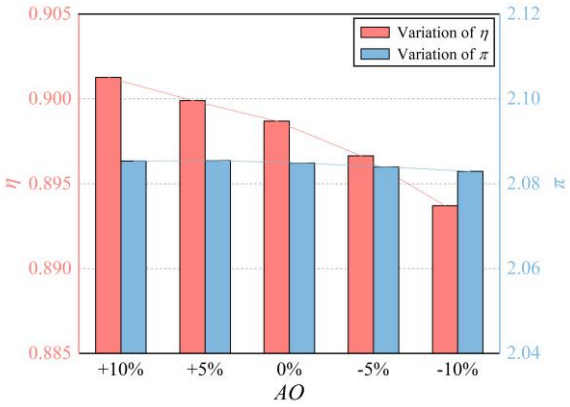

Figure 6 The performance of fan stage with different *AO* at *PE*

The high-throughflow fan consisted of two domains, which were the tandem rotor domain and stator domain respectively. Therefore, the performance of the overall stage was depended on two aspects. Figure 7 showed the performance curves of tandem rotor. It could be observed that the performance curve of tandem rotor at NC did not show obviously blockage, indicating that the throat of the overall stage was located in the stator passage. Consistent with the trend of the overall stage performance curve, the π and η varied obviously with reduced *AO* as well, and the variation trend demonstrated basically the same with the stage.

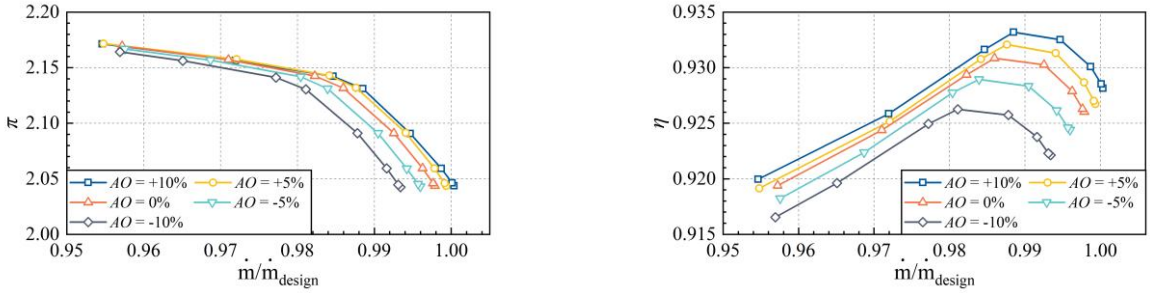

Figure 7 The performance curve of tandem rotor with different *AO*

Similar to the overall stage analysis method, we still selected the performance of tandem rotor at *PE* for comparison. The variation trend of η showed highly consistent with the overall stage, and π was insensitive with various *AO* as before. In general, the aforementioned analysis indicated that *AO* affected the overall stage performance by mainly affecting the tandem rotor performance. Therefore, to investigate the mechanisms of *AO* affecting the performance and internal flow structures should be focused on the tandem rotor domain.

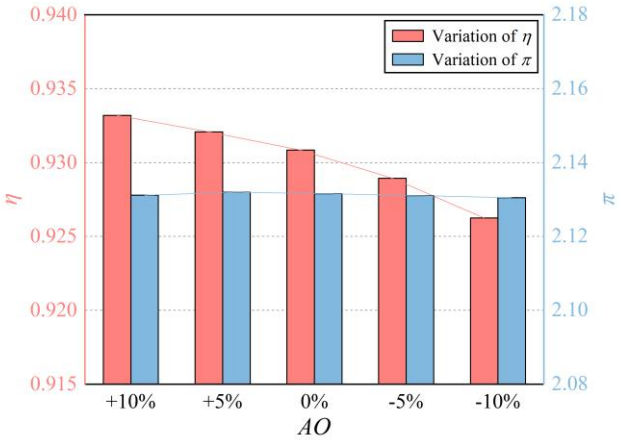

Figure 8 The performance of tandem rotor with different *AO* at *PE*

mechanisms of *ao* affecting internal flow of tandem rotor

To investigate *AO* how affected the aerodynamic performance and internal flow field of tandem rotor within high-throughflow fan, we had chosen two tandem rotors with the typical axial relative position parameters for an in-depth comparison, which were *AO* = +10% and -10%, respectively. Figure 9 demonstrated the distribution of circumferential averaged η along spanwise at outlet of tandem rotor. On the one hand, there were large-scale efficiency defects in Region A which was signed in Figure 9 with the dotted line. The span of the defects was approximately 40% to 60%, accounting for 20% along spanwise, which had a massive influence on η of tandem rotor and fan stage. On the other hand, there was an obvious difference between two tandem rotors in Region B which was signed in Figure 9 with the dotted circle and mainly existed from 70% to 80% span. In general, the axial relative position parameter *AO* had an important effect on the distribution of η, and the mechanisms of the aforementioned two phenomena would both be clarified later.

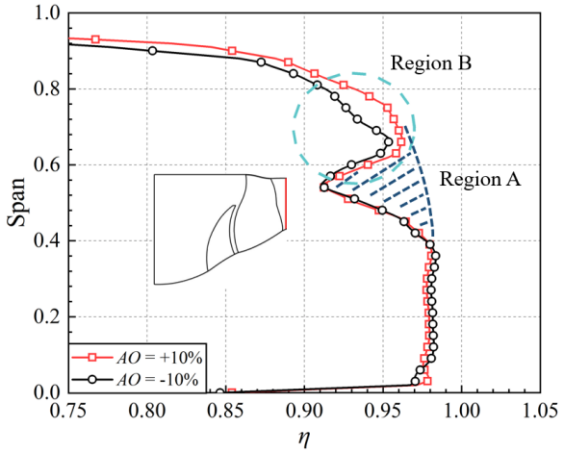

Figure 9 Distribution of circumferential averaged η along spanwise at tandem rotor outlet

The problem of efficiency defects had been clarified first. Figure 10 indicated the schematic diagram of the flow near the *BR* tip and the distribution of skin friction coefficient (C_f) on *BR SS*, and C_f was defined as

$$C_f = \tau / \left(P_{t,inlet} - P_{inlet} \right). \quad (5)$$

where τ represented the skin shear stress, $P_{t,inlet}$ represented the inlet total pressure of the fan stage, P_{inlet} represented the inlet static pressure of the fan stage. When C_f was positive, it meant the fluids flowed on the blade surface and produced friction with the skin. As C_f turned to be negative, it meant the fluids were in a separation state.

The figure showed the limitation streamlines of *BR* as well, and there was a separation line from mid-span to tip, which was coincided with the distribution of C_f. It could be observed that the separation zone caused by the shock wave/boundary layer interaction occupied a large part of the region from the mid-chord to the *TE* of *BR*, and massive low-energy fluids transported to tip along the radial direction, resulting in greater flow losses and wider wake. Zhou had mentioned in the previous paper that the vortex shedding from the *BR* tip would cause a large-scale region of high entropy. The detailed view of the tip flow also showed in the figure, and there were three main origins of the tip vortex: the first part was the low-velocity fluids of the boundary layer caused by the incoming flow passed through the tip surface; the second part was the high-velocity fluids driven by the pressure difference between the *SS* and *PS* of the *BR* tip; the third part was the aforementioned low-energy fluids of the separation region. The high-velocity fluids entrained low-velocity fluids of the other two parts to form a vortex, then propagated and diffused downstream. In conclusion, the main reasons of the efficiency defects near the mid-span of tandem rotor were due to the tip vortex and the wider wake of *BR*.

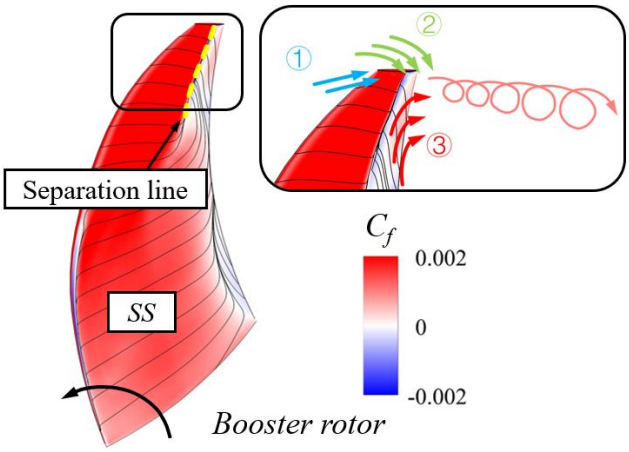

Figure 10 Flow near the tip and C_f distribution on *SS* of *BR*

The efficiency difference between the two tandem rotors mainly existed at 70% to 80% span, and the maximum difference was located at 75% span, which reached 2.65%. Therefore, B2B surface at 75% span of tandem rotor was selected for in-depth analysis. Figure 11 demonstrated the Ma_{re} contours, and due to the height of *BR* was about 60% of *FR*, there was only *FR* at the B2B surface of 75% span. From the aspect of the shock wave structure, the difference was not obvious. There was only one detached shock wave in the blade channel, and the *PS* branch formed a passage shock wave, and the *SS* branch formed a bow shock wave. As for the strength of the passage shock wave, it would be stronger when *AO* = -10% tandem rotor than *AO* = +10%. On the one hand, the denser isolines of tandem rotor with *AO* = -10% could approve the above point of view. On the other hand, the strength of interaction between the passage shock wave and

boundary layer in *AO* = -10% tandem rotor had become stronger as well, which resulted in the thickening of the boundary layer. More than that, we could observe that there was a difference in the position of the maximum velocity point of tandem rotor with different *AO*, this phenomenon would clarify later.

Further drawn the entropy contours for analysis, it could be found that there was a giant entropy-rise after the fluids passing through the shock wave when *AO* = -10%. Moreover, the high-entropy region near *SS* of *AO* = -10% tandem rotor was also extended compared with the *AO* = +10%. Therefore, the phenomena in Figure 12 confirmed the conclusions based on Figure 11, however, the deep reason why the strength of the passage shock wave was enhanced still needed analyzing further.

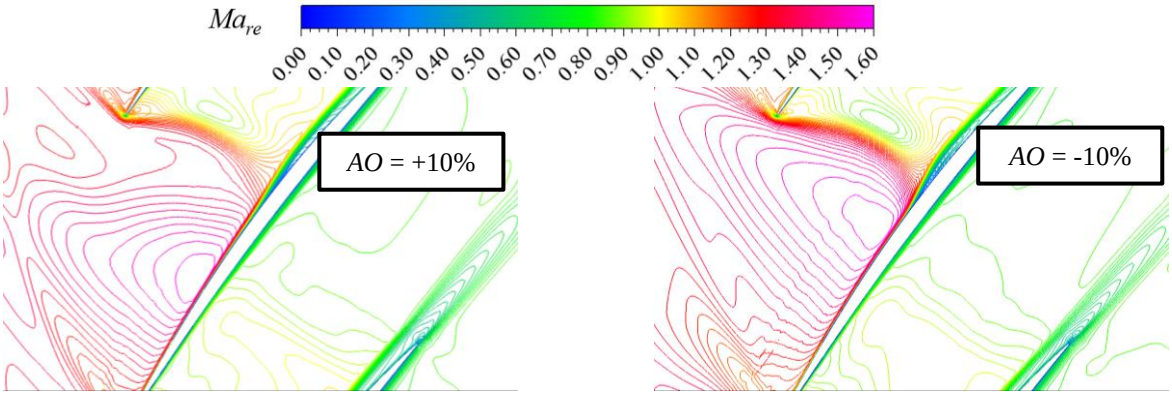

Figure 11 Ma_{re} contours at 75% span of tandem rotor

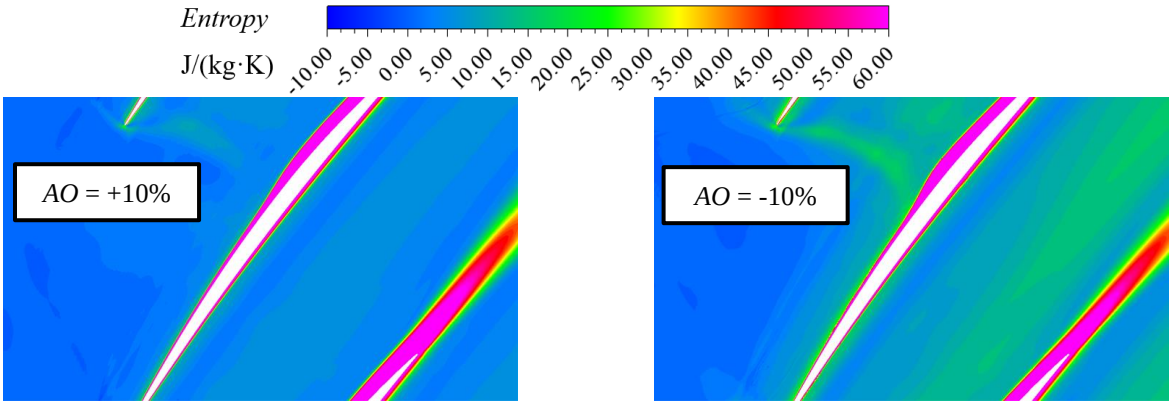

Figure 12 Entropy contours at 75% span of tandem rotor

Figure 13 showed the distribution of Ma_{re} on an S3 surface at *LE* of *FR*. Due to the axial overlap between *BR* and *FR*, *BR* would be cut off near *TE*. The black dotted circle in the figure meant the position of 75% span inlet, where the strength of passage shock wave was determined by this region. Same with the B2B surface, the isolines would become denser and Ma_{re} was enhanced when *AO* changed from positive to negative. The strength of the shock waves at the *LE* and passage was increased as the *BR* and *FR* overlapped, and airflow near the *SS* of *BR* accelerated at the inlet of *FR*. Due to higher Ma_{re}, the fluids passing through the *SS* had higher momentum that was transferred to the fluids in the upper region of the *FR* inlet due to the viscosity. Thus, the middle and upper fluids also had higher velocity, that is, the higher Ma_{re}. When the tandem rotor had an axial gap, the airflow had already passed through the *SS* of *BR* to generate a low-velocity wake before reaching the *FR* inlet. Meanwhile, the upper fluids were also partially diffused, thus Ma_{re} was decreased and became more uniform. The airflow would also be accelerated when passing through the gap between the *BR* and *FR*. Although the region of high-momentum fluids was far away from the 75% span inlet of the *FR*, the region of high Ma_{re} in the black circle would still tend to deviate toward the gap. Therefore, the accelerated fluids in the gap had a certain impact on the distribution of Ma_{re} but did not constitute a decisive factor.

In conclusion, the movement of the maximum velocity point on the *FR SS* and the change of the passage shock wave strength were both depended on the design parameter *AO*. In other words, the low-pressure potential field of the *BR SS* greatly affected the flow structures in tandem rotor domain, especially in the higher span region. As *BR* moved downstream, the effect of the potential field would become more obvious, and the strength of the detached shock wave would enhance sharply, resulting in large-scale flow separation and generating massive losses.

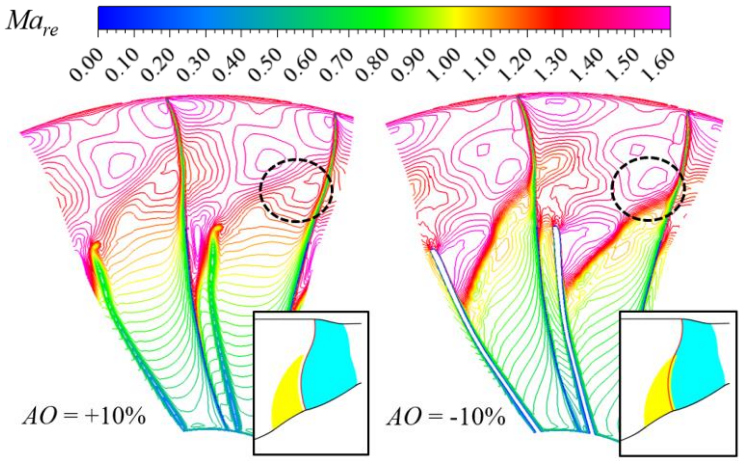

Figure 13 Contours of Ma_{re} on an S3 surface of *FR LE* in tandem rotor

CONCLUSIONS

This study applied a validated numerical simulation methodology to examine the design parameter *AO* of the tandem rotor within a high-throughflow fan. The axial matching characteristics and mechanisms of internal flow were clarified by analyzing the changes in the aerodynamic performance of tandem rotors with different configurations and the structural differences in the typical flow characteristics. This provided the foundations for engineering applications. The conclusions are as follows:

(1) The design parameters *AO* was crucial to the aerodynamic performance of the overall fan stage. Changes in the performance of the tandem rotor were highly consistent with the trend of the overall stage. Therefore, the tandem rotor had a decisive effect on the overall performance. When *PP* = 20%, the peak efficiency of the tandem rotor with a larger axial gap (*AO* = +10%) would be higher, and with the decrease of *AO*, the peak efficiency would also be reduced. The difference of stage η between the best case (*AO* = +10%) and the worst case (*AO* = -10%) reached 0.756%. Moreover, the variation of π at *PE* remained almost unchanged, which was insensitive to the parameter *AO*.

(2) From 40% to 60% span at tandem rotor outlet, there was an obvious region of efficiency defects, which resulted in a decrease in η of the fan stage and tandem rotor. To explain the above phenomenon, two main origins, which were the tip vortex and the wider wake of *BR* respectively, were obtained by analyzing the complicated flow field of the tandem rotor. The tip vortex was mainly composed of three sources, namely the low-energy fluids of the boundary layer at the *BR* tip, the high-velocity fluids driven by the pressure difference between the *SS* and *PS*, and the low-energy fluids from radial transport. The wider wake was generated by the open separation caused by the shock wave/boundary layer interaction.

(3) From 70% to 80% span, the η difference between the *AO* = +10% and *AO* = -10% tandem rotor had achieved a high level, especially at 75% span, the difference reached 2.65%. Therefore, the detailed analysis was conducted at the B2B surface of 75% span and the S3 surface at the *FR LE*. The results showed that the change of the shock wave strength in *FR* passage caused by the low-pressure potential field of *BR SS* was the main reason for the efficiency difference at 75% span. In other words, the effects of the potential field would gradually be enhanced with reduced AO, which strengthened the passage shock wave, resulting in the increase of shock wave loss and separation loss.

NOMENCLATURE

3D	three dimensional	P_t	total pressure
AO	axial overlap	*s*	circumferential distance between the chordwise extension of the *BR* and the *FR LE*
BR	booster rotor	*SS*	suction surface
C_f	skin friction coefficient	*T*	static temperature
C_x	axial chord length	*t*	blade pitch
FR	fan rotor	*TE*	trailing edge of the blade
LE	leading edge of the blade	T_t	total temperature
Ma_{re}	relative Mach number	y^+	nondimensional wall distance of the first layer
NC	near choke condition	γ	specific heat ratio
NS	near stall condition	Δx	the axial distance between the *FR TE* and the *BR LE*
P	static pressure	η	isentropic efficiency

PE	peak efficiency condition	π	total pressure ratio
PP	percent pitch	τ	skin shear stress
PS	pressure surface		

ACKNOWLEDGMENTS

The authors wish to acknowledge the financial support of the National Major Science and Technology Project of China (No.2019-II-0004-0024) and the Special Research Project of Chinese Civil Aircraft (No. MJZ-2016-D-30) for this project.

References

Li, Z., Lu, X. g., Zhao, S., Han, G., Yang, C., and Zhang, Y. (2019). 'Numerical investigation of flow mechanisms of tandem impeller inside a centrifugal compressor', *Chinese Journal of Aeronautics*, 32(12), pp. 2627-2640.

Li, Z., Han, G., Lu, X., Huang, E., and Zhao, S. (2020). 'Improving the operating range using a centrifugal compressor with a tandem impeller', *Aerospace Science and Technology*, 96, 15.

Li, Z. L., Lu, X. G., Han, G., Huang, E. L., Yang, C. W., and Zhu, J. Q. (2020). 'Numerical and experimental investigation of flow mechanism and application of tandem-impeller for centrifugal compressor'. *Aerospace Science and Technology*, 100, 18.

Guochuan, W., Biaonan, Z., and Bingheng, G. (1988). 'Experimental investigation of tandem blade cascades with double-circular arc profiles', *International Journal of Turbo and Jet Engines*, 5(1-4), pp. 163-170.

Saha, U. K., and Roy, B. (1997). 'Experimental investigations on tandem compressor cascade performance at low speeds', *Experimental Thermal and Fluid Science*, 14(3), pp. 263-276.

Li, Q. S., Wu, H., and Zhou, S. (2010). 'Application of tandem cascade to design of fan stator with supersonic inflow', *Chinese Journal of Aeronautics*, 23(1), pp. 9-14.

Brent, J., and Clemmons, D. (1974). 'Single-stage experimental evaluation of tandem-airfoil rotor and stator blading for compressors part 8: final report', NASA, CR-134713.

Burger, G., and Keenan, M. (1970). 'Single-stage evaluation of highly-loaded high-Mach-number compressor stages Part 3: Data and performance tandem rotor', NASA, CR-72772.

McGlumphy, J., Ng, W. F., Wellborn, S. R., and Kempf, S. (2010). '3D numerical investigation of tandem airfoils for a core compressor rotor', *Journal of Turbomachinery*, 132(3), 9.

Kumar, A., and Pradeep, A. M. (2020). 'Design and off-design behavior of a tandem rotor stage', *Proceedings of the Institution of Mechanical Engineers, Part G: Journal of Aerospace Engineering*, 234(4), pp. 927-942.

Mohsen, M., Owis, F. M., and Hashim, A. A. (2017). 'The impact of tandem rotor blades on the performance of transonic axial compressors', *Aerospace Science and Technology*, 67, pp. 237-248.

Murooka, T. (2007). 'Design and development of an advanced transonic fan rotor', ISABE-2007, 1136.

Zhou C., Li Z., Huang S., Han G., Lu X., Zhao S. and Zhu J. (2021). 'Numerical investigation on the aerodynamic performance and flow mechanism of a fan with a partial-height booster rotor', *Aerospace Science and Technology*, 109, 106411.